# UC Irvine

## Title

Toward a molecular understanding of the surface composition of atmospherically relevant organic particles

## Permalink

## Journal

## ISSN

## Authors

Qin, Y
Wingen, LM
Finlayson-Pitts, BJ

## Publication Date

## DOI

## Copyright Information

Peer reviewed

# Toward a molecular understanding of the surface composition of atmospherically relevant organic particles

Y. Qin[a] , L. M. Wingen[a] , and B. J. Finlayson-Pitts[a,1]

Many mass spectrometry methods using various ionization sources provide bulk composition of airborne particles, but little is known about the surface species that play a major role in determining their physicochemical properties that impact air quality, climate, and health. The present work shows that the composition of surface layers of atmospherically relevant submicron organic particles can be probed without the use of an external ionization source. Solid dicarboxylic acid particles are used as models, with glutaric acid being the most efficient at generating ions. Coating with small diacids or products from α-pinene ozonolysis demonstrates that ions are ejected from the surface, providing surface molecular characterization of organic particles on the fly. This unique approach provides a path forward for elucidating the role of the surface in determining chemical and physical properties of particles, including heterogeneous reactions, particle growth, water uptake, and interactions with biological systems.

airborne organic particles | surface sensitive mass spectrometry | inlet/vacuum ionization

For a number of decades, aerosol particles have been the subject of extensive studies in atmospheric chemistry due to their importance in air quality, human health, and global climate (1–5). Mounting evidence indicates that airborne aerosol particles are, under many atmospheric conditions, solids or semisolids (6–13), where mass transfer of the molecules into the particle can be slow (14–17). This can lead to composition differences between the surface and the core (18). Even in a liquid particle, morphological heterogeneity can occur due to liquid-liquid phase separation of organic components that are immiscible (19–21). While the surface makes up a small fraction of the particle mass, incoming gases interact at this air-particle interface first. Thus, the surface can determine how particles take up low-volatility organics to grow the particles, which must reach ~100 nm in size to scatter light and hence reduce visibility, as well as to reach the deep lung. The chemical composition of the surface will also determine its interaction with water vapor, and hence its ability to act as a cloud condensation nucleus, and it will play a role in the initial interaction of the particles with biological systems, including the respiratory tract.

Analysis of particle composition is often carried out by filter collection followed by solvent extraction and application of offline analytical techniques, especially mass spectrometry (MS). Great strides have been made using electrospray ionization MS (22, 23), chromatography, and high-resolution methods (24). Online techniques without prior collection and extraction have also been widely used. These techniques rely on a variety of methods to provide energy for generating gas-phase ions from the particles, including high voltage, laser ablation, or heating followed by electron impact or chemical ionization (25–34). However, thermal decomposition of the analytes and fragmentation during ionization can occur, making molecular characterization challenging. These techniques also give information on bulk particle composition but not information on composition of the surface separately. Techniques that are surface sensitive and preserve native molecular information are emerging but are in their infancy regarding their mechanisms and quantification (18, 35–38).

In a series of previous studies on solids, ions have been shown to form within the inlet of the mass spectrometer without an external ionization source (39–46). Such methods with no ion source are often referred to as inlet or vacuum ionization and enable molecular characterization of a variety of organic analytes with less energy input than traditional methods. For example, Trimpin and coworkers (47) first observed mass spectra directly from the sublimation of a matrix-embedded solid sample near the mass spectrometer inlet without using a laser. However, detailed understanding of the ionization mechanisms in the absence of added energy remains elusive for solids.

A variation of related methods has also been reported in which heat is used to generate ions. For example, Johnston and coworkers (44–46) have explored droplet-assisted

## Significance

Airborne particles have outsized effects on human health, visibility, and climate. While the surface makes up a small fraction of the particle mass, incoming gases interact at this interface first. Thus, the surface can determine how particles take up vapors to grow to the size that scatters light, take up water vapor leading to cloud condensation nuclei, and interact with biological systems upon inhalation. This paper describes an approach for the detection of species in the surface layers of organic particles, as opposed to the bulk species which are commonly measured. This surface sensitivity provides a path forward for understanding the role of the surface in determining particle chemical and physical properties.

Author affiliations: [a]Department of Chemistry, University of California, Irvine, CA, 92697-2025

ionization, which produces ions from micrometer-sized droplets by passing them through a heated inlet before the mass spectrometer inlet. Solvent-assisted inlet ionization is a similar method that allows analyte solution to be drawn into a heated inlet; droplets are believed to form in the vacuum region of the mass spectrometer during evaporation of the solvent (48, 49). These methods share similarities with aerodynamic thermal breakup droplet ionization methods (50–52), which have also been shown to generate ions in the mass spectrometer inlet with typical temperatures of several hundred degrees Celsius.

Here, we demonstrate that the surface composition of atmospherically relevant solid organic particles can be characterized without providing an external energy or ionization source, an approach dubbed "magic" ionization by Trimpin and co-workers (39), who demonstrated this on bulk solids. In the present studies, solid, dry glutaric acid (GA) particles, as well as the C3, C4, and C6 diacids from atomization, were used as single-component particles. In addition, GA coated with organic compounds ranging from small organic acids to high-molecular-weight compounds from α-pinene ozonolysis were studied. Mass spectra in all cases indicate the gas-phase ions originate primarily from molecules in the surface layer of the particles, providing selective characterization of the surface rather than the bulk and providing a path forward for understanding the role of particle surfaces in determining the ultimate impacts of airborne particles.

## Results and Discussion

### Production of Gas-Phase Ions from Particles without an Ionization Source.

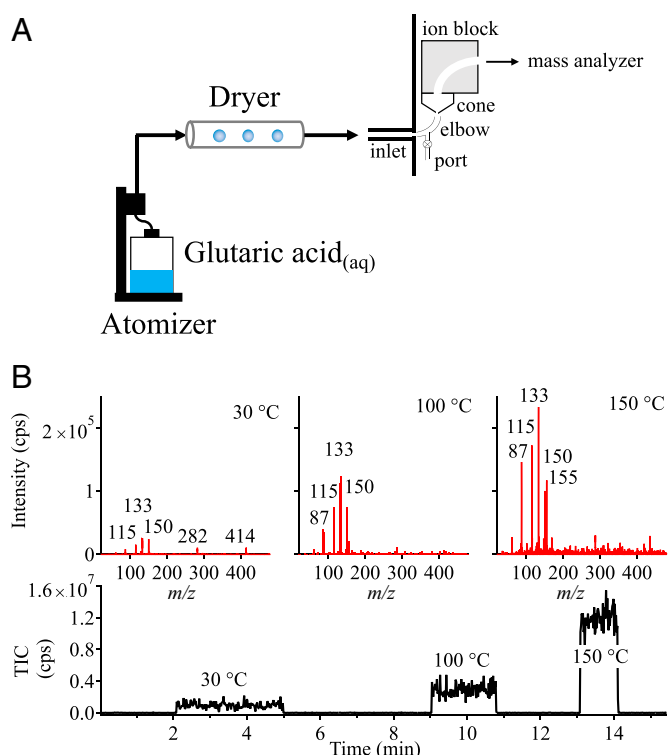Ion signals from GA particles generated using the approach in Fig. 1A in the absence of an external ionization source ($SI$ $Appendix$, Fig. S1) are shown in Fig. 1B. A clear increase in the total ion count (TIC) was observed upon introducing the stream of GA particles into the mass spectrometer, with the signal increasing with increasing temperature. The temperature is applied at the ion block (Fig. 1A) and warms the cone and ion optics but does not heat the inlet, which remains at room temperature. The major ions were at mass-to-charge-ratios (m/z) of 133, 115, and 87, corresponding to protonated GA adducts and fragments $[M + H]^+$, $[M + H - H_2O]^+$, and $[M + H - H_2O - CO]^+$, respectively. Peaks at $m/z$ 150, 282, and 414, which correspond to the ammoniated adducts of GA $[M + NH_4]^+$, $[2M + NH_4]^+$, and $[3M + NH_4]^+$, respectively, were also observed at low temperature. At higher temperatures, the $[2M + NH_4]^+$ and $[3M + NH_4]^+$ peaks disappeared, possibly due to thermal decomposition, while the sodiated adduct $[M + Na]^+$ ($m/z$ 155) survived. Ammoniated adducts are an intrinsic characteristic of ambient ionization due to ammonia in air and are also observed in other ambient ionization methods, such as direct analysis in real time (DART) MS (53). The sodiated adduct originates from trace metals in the glassware (54). In all cases, the signal returned to near-zero background levels when the particle stream was removed from the inlet region.

This experiment clearly shows that gas-phase ions are produced from the particles without an external ionization source. The results are similar to reports by Trimpin and coworkers (39–43, 47, 55) that sublimation of samples in the presence of a matrix compound yields mass spectra of the analytes. These results are also consistent with the observations from solvent-assisted inlet ionization and droplet-assisted ionization that gas-phase ions are produced without an external ionization source (44–46, 49–52).

Experiments were carried out using size-selected GA particles in which the number, surface area, or volume concentrations were held constant while varying the diameter. In these experiments, the ion signal was significantly smaller due to the much lower number concentrations, for size-selected particles [$(3 − 7) \times 10^4$ cm$^{-3}$] versus polydisperse particles ($\sim 2 \times 10^6$ cm$^{-3}$). Thus, the more sensitive multiple reaction monitoring (MRM) method, which monitored the ion signal for the transition $m/z$ 133/115, was used for size-selected GA particles.

Fig. 2 shows the ion signal intensities observed for diameters ranging from $\sim$80 to 270 nm, with data points colored by surface area concentration. When the number concentration was held constant (Fig. 2A), the signal increased for larger diameters. However, the ion signal was constant for increasing diameters when their surface area concentration was held constant (Fig. 2B), suggesting that the particle surface area plays a major role in ion generation. Finally, when the volume concentration was held constant (Fig. 2C), the signal decreased as the diameter increased. All of the data points from Fig. 2 plotted together ($SI$ $Appendix$, Fig. S2) demonstrate that the signals depend on the surface area of the particles.

### Molecular Ion Ejection near the Surface of Core-Shell Particles.

Ions originating from sublimation will come from the outer surface layers of the particle (56, 57). To examine this further, size-selected GA particles were coated with different coating thicknesses by condensation of vapors from other diacids. Fig. 3A shows the results for GA particles coated with adipic acid (AA), in which the core $[GA + H]^+$ and the coating $[AA + H]^+$ signals are plotted as functions of coating thickness. The coating thickness was measured from changes in the particle size distribution as the coating temperature increased ($SI$ $Appendix$, Fig. S3). As the coating layer increased from 0 to 10 nm, the AA



**Fig. 1.** (A) Schematic of the apparatus in which GA particles were sent directly to the mass spectrometer without an external ionization source. (B) Typical time series of the TIC (black trace) and the corresponding mass spectra (red traces). The particles were sampled at 2 to 5, 9 to 11, and 13 to 14 min, with ion block temperatures of 30, 100, and 150 °C, respectively. aq, aqueous solution; cps, counts per second.
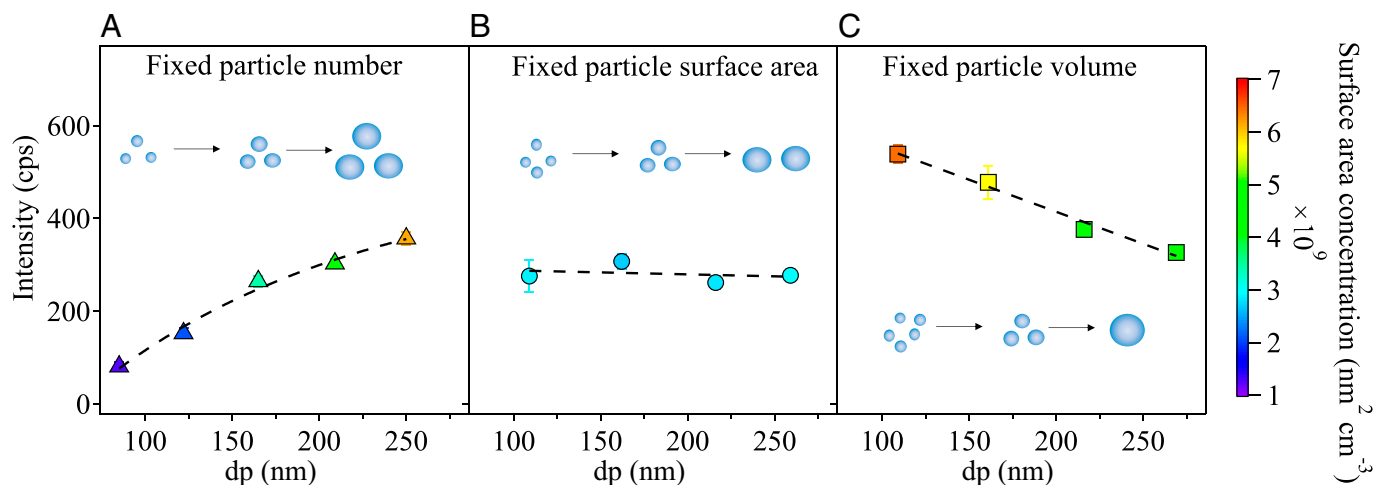
**Fig. 2.** Signal intensity of size-selected GA particles as a function of particle diameter ($d_p$) in experiments with fixed (*A*) number concentration (triangles), $(3.2 \pm 0.7) \times 10^4$ cm$^{-3}$ (*B*) surface area concentration (circles), $(2.9 \pm 0.1) \times 10^9$ nm$^2$ cm$^{-3}$, and (*C*) volume concentration (squares), $(2.1 \pm 0.05) \times 10^{11}$ nm$^3$ cm$^{-3}$. The uncertainties in intensity are similar to the size of the symbols.

coating signal increased while the GA core signal decreased, consistent with ions originating from the surface AA molecules. These surface molecules shielded the underlying GA, suppressing its sublimation. However, both GA and AA signals dropped with a further increase in coating thickness (>15 nm). Similar results were observed using dodecanedioic acid (DA) as the coating (Fig. 3*B*). Clearly, sublimation of the GA core enhances ejection of compounds from the surface. The DA signal decreases at a thinner coating than that in the AA coating experiment, perhaps due to the lower vapor pressure of DA. In short, the results indicate that sublimation of the GA is one of the key components in generating the ion signals, with efficient ion formation for molecules in the particle surface layers.

To test whether the ionization method works for atmospherically relevant multicomponent coatings, dry GA particles were coated with secondary organic aerosol (SOA) formed from α-pinene ozonolysis generated in a flow reactor. For comparison, SOA particles alone were also generated by self-nucleation without the GA seed. In addition, separate streams of self-nucleated SOA and atomized GA particles were analyzed. As shown in Fig. 4*A*, the SOA particles alone yielded an insignificant signal. Introducing two separate streams of SOA and GA particles gave GA ions but no SOA signal (Fig. 4*B*). However, for the SOA-coated GA particles, both GA and SOA were detected (Fig. 4*C*). Peaks due to typical products of α-pinene ozonolysis were observed, such as pinonic acid (22, 23, 58, 59).

Significant signals were also observed for high-molecular-weight compounds ($m/z > 300$). A comparison to mass spectra obtained using DART-MS is shown in *SI Appendix,* Fig. S4. A higher proportion of high-molecular-weight compounds was observed in the spectra from magic ionization than that in the DART spectra. Since DART requires the use of high temperatures to vaporize solid analytes, it is likely that the high temperatures either decomposed some of the high-molecular-weight compounds ($m/z > 500$) or were not high enough to vaporize the high-molecular-weight, highly oxygenated molecules. The spectra in Fig. 4 support the role of GA particles in enhancing sublimation of surface compounds with high molecular weights and/or low vapor pressures.

A further reverse experiment was conducted to coat the self-nucleated SOA with GA. Signals from both the SOA core and GA were very small (*SI Appendix,* Fig. S5*A*), showing that GA is much more effective in generating an SOA spectrum when it is used as the core (Fig. 4*C* and *SI Appendix,* Fig. S5*B*). This supports the sublimation of the charged GA as the key; when GA is in the core, it can carry species above it into the gas phase, while as a coating, it is unable to carry along the underlying SOA.

The SOA coating was varied by using different initial α-pinene concentrations, from 2 to 40 ppm. As shown in Fig. 5, the TIC decreased from $3.5 \times 10^7$ to $2.3 \times 10^7$, $1.7 \times 10^7$, and then $0.7 \times 10^7$ cps with an increase in the α-pinene concentration. The higher α-pinene concentrations lead to a thicker coating



**Fig. 3.** (*A*) Intensities from size-selected GA particles coated with AA formed by condensation of the vapor as a function of coating thickness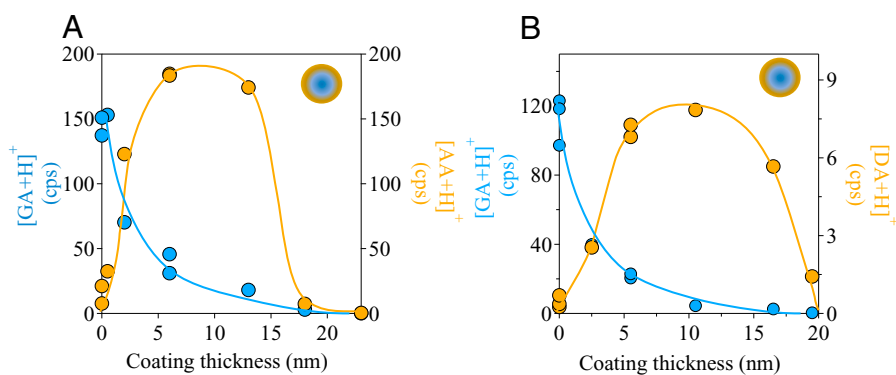. (*B*) Intensities from size-selected GA particles coated with DA formed by condensation of the vapor as a function of coating thickness. For each system, the signal intensities plotted correspond to the parent molecular ions [GA + H]$^+$, [AA + H]$^+$, and [DA + H]$^+$. Blue symbols show the core, and orange symbols show the coating.

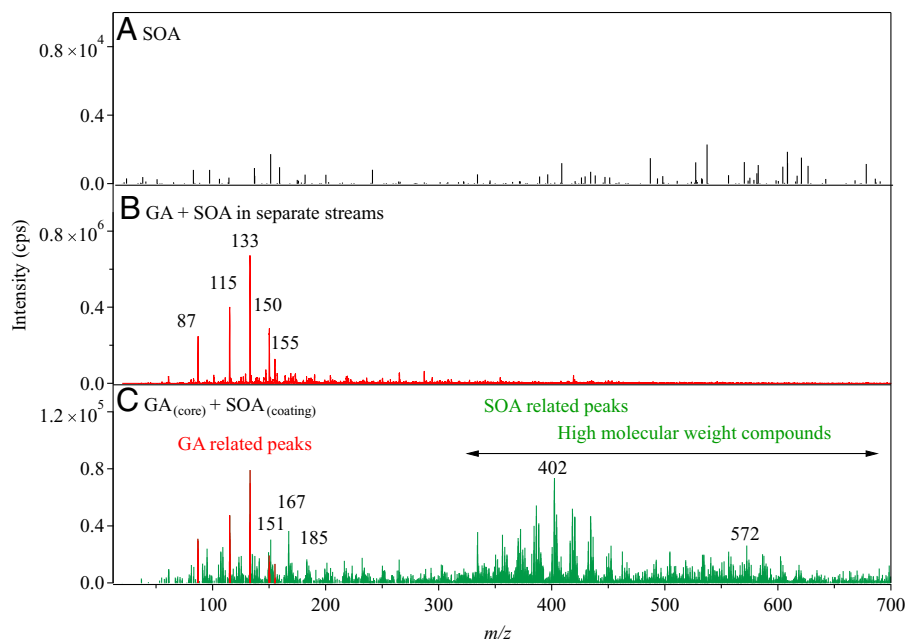https://doi.org/10.1073/pnas.2209134119

**Fig. 4.** Mass spectra of (*A*) self-nucleated α-pinene SOA alone, (*B*) atomized GA particles and self-nucleated α-pinene SOA in separate streams, and (*C*) atomized GA particles coated with α-pinene SOA. Note the different intensity scales.

of the GA core, which suppresses the sublimation of the GA core and the intensity of the signals from the surface species. These results are consistent with the results of the single-compound coatings, which show that sublimation of GA plays an important role in generating the ion signals. While the total signal intensity decreased, the shell-to-core (SOA-to-GA) ratio, obtained from the sum of all SOA peaks ratioed to the sum of all GA peaks, increased (*SI Appendix,* Fig. S6). This result further demonstrates that ions are ejected preferentially from the particle surface.

This surface ionization occurred for other core particles as well. For example, *SI Appendix,* Fig. S7 shows a clear signal from AA core particles coated with SOA, although longer collection times were required to give a signal comparable to that from GA core particles. The experiments demonstrate the utility

of this magic ionization method for surface analysis of particles on the fly, where compounds with a variety of vapor pressures and molecular weights are present.

**Activation Energy for Ion Generation.** The activation energy ($E_a$) for ion generation was measured for uncoated GA particles with different charge densities formed using three different processes: 1) atomization from solution, 2) self-nucleation from the gas phase, and 3) self-nucleation followed by exposure to ions formed by passing self-nucleated particles through a Po-210 neutralizer. Particles generated by atomization hold more charges than those from self-nucleation (60–62). Particle charging during atomization occurs via frictional forces known as spray electrification; this effect is illustrated by the intense electrification of water droplets in waterfalls (63). To increase the charge on the self-nucleated
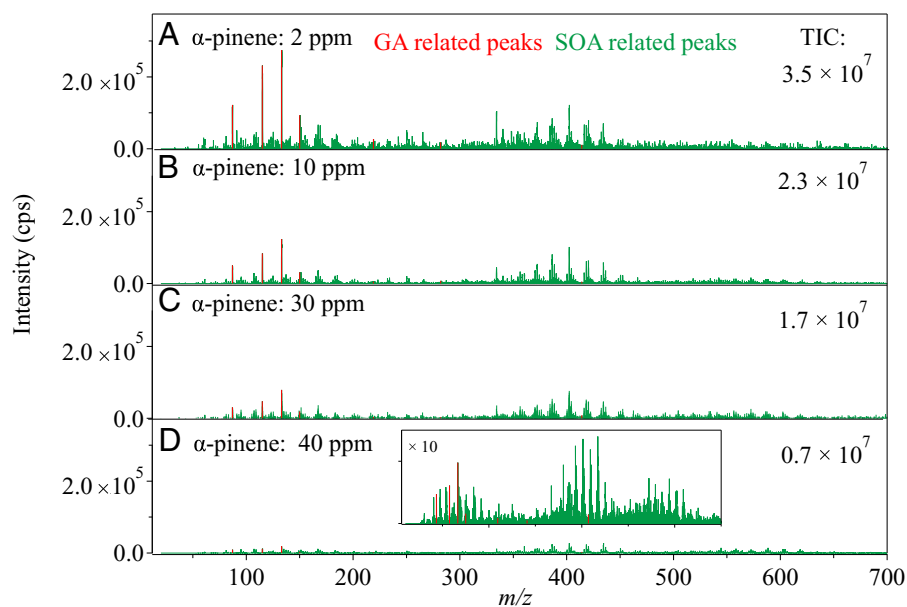


**Fig. 5.** Mass spectra of SOA-coated GA particles with increasing SOA coating obtained by increasing the initial α-pinene concentration from 2 to 40 ppm. The inset shows the spectrum in *D* scaled by 10×.
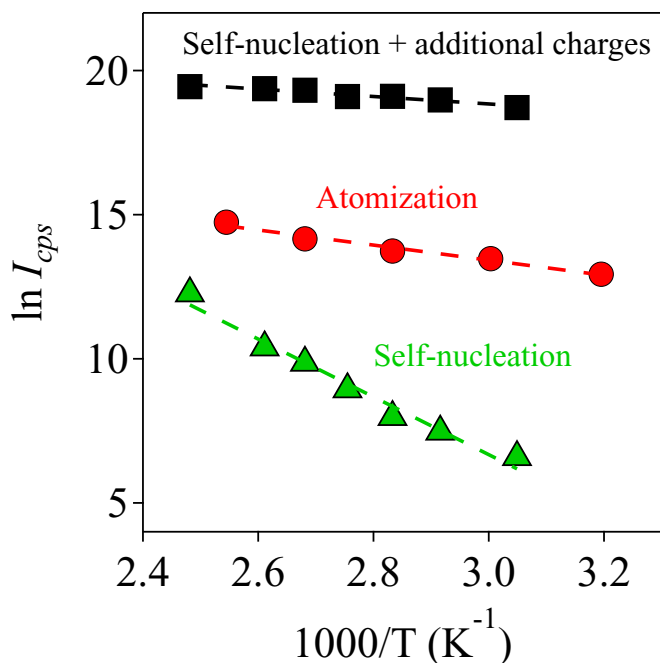
**Fig. 6.** Arrhenius plots of the sum of ions from GA particles from atomization, self-nucleation, and self-nucleation with Po-210. The slopes of the plots give $E_a$ = 22 ± 2 kJ mol$^{-1}$ for ions from atomization, $E_a$ = 83 ± 6 kJ mol$^{-1}$ for ions from self-nucleation, and $E_a$ =11 ± 1 kJ mol$^{-1}$ for ions from self-nucleation with additional charges using Po-210. Dashed lines are fits by least-squares regression. The sum of ions includes [GA+H]$^+$, [GA+H-H$_2$O]$^+$, and [GA+H-H$_2$O-CO]$^+$. Signals for [GA+NH$_4$]$^+$ and [GA+Na]$^+$ were variable and are not included in the TIC. When included, $E_a$ for the total ions becomes 19 ± 1, 83 ± 6, and 11 ± 1 kJ mol$^{-1}$, respectively.

particles, the particles were exposed to a Po-210 neutralizer, where charging occurs by random collisions between the ions and the particles before they enter the mass spectrometer (64).

Fig. 6 shows Arrhenius plots of total ions from the protonated GA and its associated fragments [GA+H-H$_2$O]$^+$ and [GA+H-H$_2$O-CO]$^+$. $E_a$ was obtained from the slope of plots of ln (ion signal intensity) versus T$^{-1}$, where the total ions were followed as a function of the applied ion block temperature. The Arrhenius plots and the derived $E_a$ of each individual ion are shown in *SI Appendix*, Fig. S8 and *SI Appendix*, Table S1. Ions from atomized GA had a significantly lower $E_a$ (22 ± 2 kJ mol$^{-1}$) than those generated from self-nucleation (83 ± 6 kJ mol$^{-1}$). Furthermore, the additional charges from applying the Po-210 on the self-nucleated GA lowered the $E_a$ rather dramatically, to 11 ± 1 kJ mol$^{-1}$. These values correspond to enthalpies of 19, 80, and 8 kJ mol$^{-1}$ for atomized, self-nucleated, and self-nucleated particles with additional charges, respectively. These are all lower than the sublimation enthalpy of neutral GA (130 ± 11 kJ mol$^{-1}$) (65). Lower enthalpies (100 ± 5 kJ mol$^{-1}$) have been reported for GA particles that are in the form of supercooled liquids, which tend to behave similarly to amorphous solids (65). Whether the particles generated here are crystalline or amorphous is unknown. Nevertheless, the lower $E_a$ for particles with higher charge densities suggests that enhanced sublimation with a lower energy barrier occurred due to the charges on the particles. This may also be responsible for the enhanced surface signals observed in orthogonal mode, sonic spray MS (38). A related observation by Johnston and coworkers (44) during droplet-assisted ionization is that the $E_a$ of ion formation for nonionic solutes in aqueous solutions was about equal to the enthalpy of vaporization of water but much smaller for salt droplets, which, as they dry, may be similar to the solids studied here.

**Proposed Mechanism of Ion Generation from Particles.** When particles enter the mass spectrometer, the diameter rapidly decreases under sub-atmospheric pressure and, in some experiments, higher ion block temperatures. This shrinkage will increase the charge density on the particle surface. Direct probing of the particle diameter change under vacuum conditions within the mass spectrometer was not possible. However, changes in particle diameter could be measured after the inlet at the elbow (Fig. 1A). The ion block heats the particles as they travel into the mass spectrometer, and this also heats the elbow to some extent. Particles were size selected with a fixed diameter of 162 nm at room temperature and atmospheric pressure. The mode diameter of the particles decreased to 146 nm at 38 °C measured at the elbow and further to 109 nm at 61 °C (Fig. 7). The measured reduction in the diameter can be viewed as a lower limit since the particles are expected to undergo more evaporation with the increased temperature and decrease in pressure in the ion block and in the ion optics inside the mass spectrometer.

As the particle diameter decreases, repulsion between the charges increases. Mechanisms of ion formation from liquid droplets where solvent evaporation increases the repulsive forces between charges on the surface have been explored in detail (66–75). Formation of gas-phase analyte ions occurs via two processes: Coulombic fission and ion evaporation. For larger droplets, Coulombic fission dominates, in which the charge density on the surface builds up during shrinkage of the droplet to the point that Coulombic repulsion causes ejection of smaller charged droplets and is known as the charged residue mechanism (CRM) (66–75). At smaller sizes, ~10 to 40 nm (67), below but still near the Rayleigh limit, conical shape fluctuations on the droplet surface provide the escape route for ion emission into the gas phase. The single-ion emission below the Rayleigh limit is known as the ion evaporation mechanism (IEM) (66–75). In the experiments reported here, the particles are solids, but similar driving forces for ion generation may occur. The ejection of



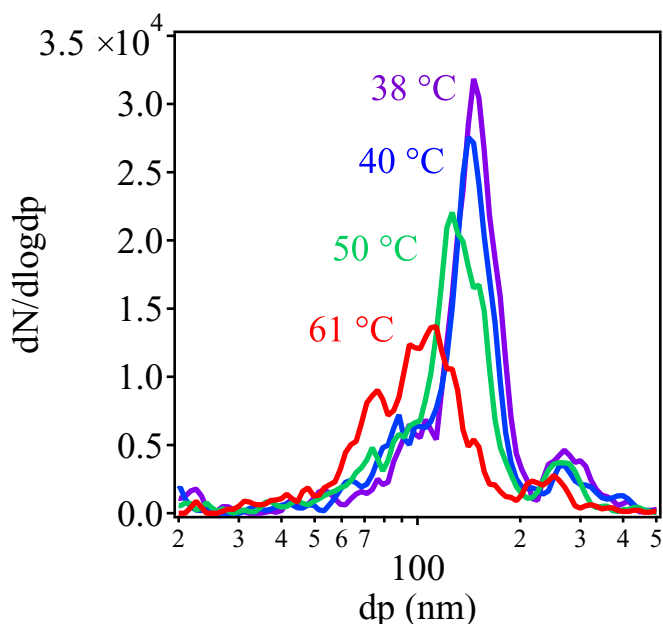**Fig. 7.** Size distributions of GA particles at different ion block temperatures measured at the port in the elbow in the inlet region (Fig. 1 and *SI Appendix*, Fig. S1). The temperature of the elbow at which the size distribution was measured for the purple, blue, green, and red lines was 38, 40, 50, and 61 °C, respectively. dN/dlogdp is the particle number concentration (N) normalized to the bin width of d$_p$.

charged particles in magic ionization of bulk solids has been proposed (39–43, 47, 55) although particles have not been directly observed. For the set of experiments in Fig. 7, the particles were generated in the same manner with the same initial diameter, so the initial charges they carried before entering the mass spectrometer were the same. However, when they entered the mass spectrometer inlet, the heating of the elbow and the ion block led to shrinking of the initial diameter. As predicted by the CRM and IEM models, this shrinking led to a decrease of the particles' ability to hold the charges, which further led to the ejection of ions to the gas phase and their detection in the mass spectrometer. The ion signals detected as shrinking proceeded from the experiment were reasonably well matched by both the CRM and the IEM models (*SI Appendix*, Fig. S9 and *SI Appendix*, Text S1).

The CRM and IEM models apply to liquid droplets where ejection of highly charged droplets from low-viscosity solvents occurs readily (74). In addition, exchange between the surface of the droplet and the interior is relatively fast. This is less likely with the solid particles used here; however, solid particles contain surface defects in the form of steps and edges. It is from these locations that sublimation preferentially occurs (56) and is likely the source of ion formation as well.

The ion signals were not unique to GA particles. Atomization and drying of malonic acid, succinic acid, and AA to form particles also yielded clear ion signals and mass spectra, although they were generally smaller than for GA by a factor of ∼20 to 30 (*SI Appendix*, Fig. S10). A mechanism based solely on sublimation to generate ions would be expected to show dependence on the sublimation enthalpy and vapor pressures of the compounds. However, a trend of ion signals with enthalpies or vapor pressures was not evident here (*SI Appendix*, Fig. S10).

GA gave the highest signal, which may reflect more surface irregularities from which sublimation can occur. Charges may begin to concentrate at these irregular locations as shrinking proceeds, leading to a Coulombic-type fission or ion emission from sites where the molecules are less strongly bound than in the bulk solid. In this regard, it is noteworthy that theoretical calculations show that the binding energy of one GA molecule to another might be as low as 90 kJ mol$^{-1}$, similar to the $E_a$ for ion formation measured here for self-nucleated GA (76).

An additional set of experiments was conducted to quantify the proportion of multiple charges held for malonic acid, succinic acid, GA, and AA particles, which represents the C3-C6 diacid series. Particles were atomized and dried as before but directly flowed into an electrostatic classifier without passing through a neutralizer. The removal of the neutralizer is to allow the particles to retain the charge states they acquire during atomization. At a fixed voltage, particles entering the electrostatic classifier with different charges would come out at different sizes but the same electrical mobility, which can be measured by a scanning mobility particle sizer (SMPS) placed downstream. Examples of the GA and AA particles with different sizes at a fixed voltage of −493 V (corresponding to a singly charged particle diameter of 100 nm) are shown in Fig. 8 *A* and *B*. A significant fraction of the particles have multiple charges. This is expected for particles experiencing spray electrification (63). However, GA retains a higher proportion of multiple charges than the other diacids (Fig. 8*C*). The multiple-charge proportion of the GA particles may be underestimated for GA here, as the GA particles have undergone significant shrinking, which is evident in Fig. 8*A*, and have thus potentially already ejected some of the charges to the gas phase. These multiple-charge measurements are consistent with the observations that GA gave the highest signal and that
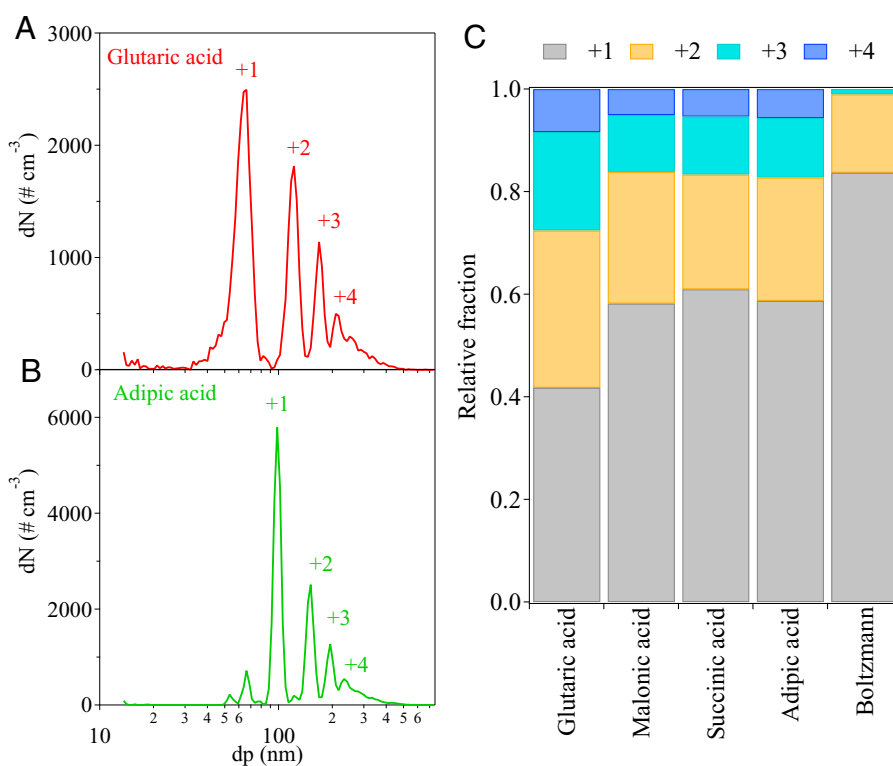


**Fig. 8.** (*A*) Size distribution of the size-selected GA particles with multiple charges from atomization. (*B*) Size distribution of the size-selected AA particles with multiple charges from atomization. (*C*) The relative fraction of the multiple charges for the size-selected diacid particles from atomization for the C3-C6 diacids. The relative fraction is estimated from the peak height in the size distribution. The relative fraction of multiple charging given by the Boltzmann equilibrium is also plotted (64).

the effective $E_a$ for ion production was lower for the atomized particles (22 kJ mol$^{-1}$) compared to the self-nucleated particles (83 kJ mol$^{-1}$).

Thermal gradients in the particles will occur due to sublimation from the surface, and such gradients have been proposed to drive excess charges to the surface (77, 78). Although larger ions are not expected to be mobile in a solid such as GA, transfer of a proton may be faster in the diacids through a Grotthuss type of mechanism in which protons diffuse through the hydrogen bond network between the molecules (79, 80). GA has acid dissociation constants similar to those of other acids such as succinic acid and AA, so enhanced deprotonation of GA seems unlikely. However, it is possible that there is faster proton migration in GA compared to the other dicarboxylic acids. Another contributing factor to increased mobility of ions in solids may be a decrease in particle viscosity with particle size. For example, the viscosity of SOA from α-pinene falls for sizes below 100 nm (81). The size distributions of the particles in the current study include a significant number below 100 nm (Fig. 7 and *SI Appendix*, Fig. S11). Similar to work by Trimpin et al. (41), the ion yields per surface area of the particle population in this study were small (~$10^{-6}$ or less) (*SI Appendix*, Fig. S10). Thus, the ions formed from solid particles may come primarily from protons at surface defects in the smallest particles, where transport to the defects is aided by lowered viscosity compared to larger particles.

In summary, it has been demonstrated that molecular components of the surface of atmospherically relevant organic aerosol particles can be uniquely identified on the fly without an ionization source. Significant advantages of this approach are its surface sensitivity, near-zero background, rapid response, and minimal decomposition of the analyte. A number of processes are controlled by the composition of the surface of particles, including heterogeneous reactions, particle growth, water uptake, and interactions with biological systems. As an example, the method can be used to study the condensed-phase oxidation of solid or semisolid particles, in which reactions that occur on/at the surface may differ from those in the bulk or in the gas phase. It can also be used to study changes in the surface composition that alter the uptake of water and other gas-phase molecules. Such molecular changes at the surface can be related back to processes controlling particle growth or their ability to act as cloud or ice condensation nuclei. It may also be used to study the formation of high-molecular-weight species during oxidation of different gas-phase organic compounds since the products are expected to condense onto the particles. In short, this study provides a path forward for understanding the surface composition of, and gas partitioning to, organic airborne particles and hence for understanding the role of the surface in determining chemical and physical properties of particles and their impacts on air quality, visibility, and climate.

## Methods

### Mass Spectrometry with No Ionization Source.
Mass spectra were collected on a triple-quadrupole mass spectrometer (Waters, Xevo TQ-S) with the ion source removed. A blank ion source housing door was used that contained only a 1/4-inch inlet. Sample flow was guided from the ambient laboratory atmosphere into a ceramic tube inlet through a short metal elbow (Vapur interface) to the spectrometer's cone, as shown in Fig. 1 and *SI Appendix*, Fig. S1. A small port in this elbow allowed particle size distributions to be collected with an SMPS. In some experiments, the ceramic inlet was removed; no change was observed in mass spectra or signal intensity.

The temperature-controlled ion block (source temperature) was typically operated at 150 °C and was varied in separate experiments to examine the temperature dependence of ion signals between 30 and 150 °C. This ion block heats the sample as it travels through the cone into the vacuum region and ion guide before the first quadrupole. This also heats the elbow and the particles to some extent before they enter the vacuum region. Separate measurements of elbow temperature were made using an infrared thermometer (Etekcity, Lasergrip 774); the temperature of the elbow varied from 38 to 61 °C.

Mass spectra were obtained using a cone voltage of 30 V and a source offset of 50 V. Increases in the cone and source offset potentials induced some ion fragmentation but did not have a significant effect on overall total ion signals. Positive ion mode mass spectra were collected in continuum or multichannel analysis (MCA) mode from *m/z* 20 to 700, or using single ion recording (SIR) or MRM scans, with ion dwell times of 0.5 s depending on the experimental conditions described below. SIR and MRM scans are techniques widely used for their high sensitivity. In the SIR scans, the mass spectrometer is set to monitor the intensity of specific *m/z* values. In MRM scans, an ion of a particular *m/z* value is selected in the first quadrupole, and its product ions after collision-induced dissociation are detected in the second quadrupole. Some mass spectra were collected over longer periods of time and in MCA mode to improve signal-to-noise ratios.

### DART-MS.
DART-MS was carried out using a DART ionization source (IonSense) equipped with the Vapur interface connected to the same mass spectrometer and ceramic inlet tube. To collect spectra in which SOA was sampled on its own or used as a coating on GA particles, the gas-phase α-pinene ozonolysis products were first removed by passing the particles through a denuder. The remaining particle stream was exposed to a temperature of 150 °C prior to sampling with DART to vaporize the particles.

The DART probe distance was 4 cm from the inlet. Mass spectra were collected in positive ion mode and averaged over 2 min in the range of *m/z* 20 to 700. Background spectra were also recorded by measuring room air and subtracting from particle spectra. DART was operated with helium reagent gas at a flow of 3.1 L min$^{-1}$, a helium gas temperature of 300 °C, and a grid electrode voltage of 350 V.

### Generation of Polydisperse Atomized GA Particles.
A schematic of the apparatus for the generation of polydisperse GA particles is shown in Fig. 1*A*. A solution of 20 mM GA (Sigma-Aldrich, 99%) in 18.2 MΩ cm of water (Milli-Q, Millipore Corporation) was atomized at a flow rate of 3.5 L min$^{-1}$ with zero air using a constant output atomizer (TSI, model 3076). The atomized GA particles were passed through two silica gel diffusion dryers, which resulted in low relative humidity (<5%). Size distributions of the particles were measured using an SMPS (TSI) consisting of an electrostatic classifier (model 3080), a long differential mobility analyzer (DMA) (model 3081), and a condensation particle counter (model 3776). The SMPS was operated with a sheath flow of 3 L min$^{-1}$ and an aerosol flow of 0.3 L min$^{-1}$. A typical size distribution of polydisperse GA particles is shown in *SI Appendix*, Fig. S11.

### Generation of Size-Selected Atomized GA Particles.
A portion of polydisperse GA particles was passed through a DMA (TSI, model 3081) for particle size-selection experiments. The particle flow through the DMA was 1 L min$^{-1}$. During size selection, evaporation of the GA particles inside the DMA was observed. For example, even with the 3:1 ratio, a selected mode diameter of 200 nm yielded a mode diameter of 161 nm measured with an SMPS downstream (TSI, model 3938). Similar evaporation has been observed previously in this and other laboratories (38, 82, 83). A schematic of the apparatus is shown in *SI Appendix*, Fig. S12*A*. Experiments in which the particle number concentration was held constant while the diameter was varied (Fig. 2) were achieved by adjusting the sheath airflow rate in the DMA. A similar procedure was used to hold the surface area and volume concentrations of particles constant for different diameters. SIR or MRM scans were used to collect mass spectra in size-selection experiments due to lower particle number concentrations.

### Generation of Polydisperse Self-Nucleated GA Particles.
The schematic for the generation of self-nucleated GA particles is shown in *SI Appendix*, Fig. S12*B*. Pure GA solid was placed in the reservoir of a T assembly with 0.35 L min$^{-1}$ air flowing over the solid. Another flow of 6 L min$^{-1}$ air was

directed into the top of the T assembly, giving a total flow of 6.35 L min$^{-1}$ air exiting the coater. The reservoir temperature was controlled with heating tape and a variable transformer. The temperature in the reservoir for the self-nucleated GA particles was 130 °C, measured with a thermocouple (Omega, type K). SIR scans were used to collect mass spectra due to the low signals in these experiments.

**Generation of Size-Selected GA Particles Coated with Diacids.** Size-selected GA particles were coated with either AA or DA using the coating assembly shown in *SI Appendix*, Fig. S12C. Pure AA solid (Sigma-Aldrich, ≥95%) or DA solid (Sigma-Aldrich, 99%) was placed in the reservoir of the coating assembly with 0.35 L min$^{-1}$ air flowing over the solid. Size-selected GA particles flowed at 1 L min$^{-1}$ through the top of the assembly, giving a total flow of 1.3 L min$^{-1}$ exiting the coater. The temperature in the coating reservoir controlled the coating thickness, and an SMPS was used to measure corresponding increases in diameter, as shown in *SI Appendix*, Fig. S3.

**Generation of Self-Nucleated SOA Particles.** Self-nucleated SOA particles were generated in a flow reactor with α-pinene ozonolysis, as shown in *SI Appendix*, Fig. S12D. Gas-phase α-pinene was generated by injecting the pure liquid (Sigma-Aldrich, ≥99%) into a 0.1 L min$^{-1}$ flow of clean air using an automated syringe pump. Ozone, produced by passing a flow of 0.3 L min$^{-1}$ air through a Pen-Ray mercury lamp (model 11SC-2), was added to the flow reactor. A flow of 3.5 L min$^{-1}$ dry air was added to the flow reactor to give a total flow of 3.9 L min$^{-1}$ and a residence time of 22 s. The initial O$_3$ concentration was 5 ppm, measured using an ultraviolet-visible spectrometer (Ocean Optics, HR4000). The initial concentration of α-pinene varied from 2 to 40 ppm. A carbon denuder was placed after the flow tube to remove the gas-phase products and any unreacted reactant. Mass spectra were collected in continuum mode scanning from *m/z* 20 to 700, with an average collection time of 5 min.

**Generation of Polydisperse GA Particles Coated with SOA.** Polydisperse GA particles were coated with α-pinene SOA generated in the apparatus shown in *SI Appendix*, Fig. S12D. The polydisperse GA particles flowed into the flow reactor at 3.5 min$^{-1}$, with ozone and α-pinene also flowing in at varying concentrations in air. Gas-phase α-pinene and ozone were injected in the same manner as described above. Diameter increases were not detectable with polydisperse GA particles because of the large width of the size distributions. Mass spectra were collected in continuum mode from *m/z* 20 to 700, with an average collection time of 5 min.

**Generation of Size-Selected GA Particles with Multiple Charges.** To examine multiple charging on particles generated from several diacids, particles were atomized and dried as described above and then flowed into a first electrostatic classifier (DMA) from which the neutralizer had been removed (*SI Appendix*, Fig. S12E). The removal of the neutralizer allowed the particles to retain the charge states they acquired during atomization. At a fixed voltage, singly and multiply charged higher mass particles with equal electrical mobilities exit the first DMA, and their diameters are measured by an SMPS downstream. The voltage in the first DMA was −493 V, corresponding to a singly charged diameter of 100 nm, with a sheath flow of 3 L min$^{-1}$ and sample flow of 1 L min$^{-1}$.

1. M. Hallquist *et al.*, The formation, properties and impact of secondary organic aerosol: Current and emerging issues. *Atmos. Chem. Phys.* **9**, 5155–5236 (2009).
2. C. L. Heald, J. H. Kroll, The fuel of atmospheric chemistry: Toward a complete description of reactive organic carbon. *Sci. Adv.* **6**, eaay8967 (2020).
3. G. Myhre *et al.*, Modelled radiative forcing of the direct aerosol effect with multi-observation evaluation. *Atmos. Chem. Phys.* **9**, 1365–1392 (2009).
4. O. B. France *et al.*, "Clouds and aerosols" in *Climate Change 2013: The Physical Science Basis. Contribution of Working Group I to the Fifth Assessment Report of the Intergovernmental Panel on Climate Change*, T. F. Stocker *et al.*, Eds. (Cambridge University Press, Cambridge, 2013), pp. 571–658.
5. J. E. Thompson, Airborne particulate matter: Human exposure and health effects. *J. Occup. Environ. Med.* **60**, 392–423 (2018).
6. A. Virtanen *et al.*, Bounce behavior of freshly nucleated biogenic secondary organic aerosol particles. *Atmos. Chem. Phys.* **11**, 8759–8766 (2011).
7. A. Virtanen *et al.*, An amorphous solid state of biogenic secondary organic aerosol particles. *Nature* **467**, 824–827 (2010).
8. C. Kidd, V. Perraud, L. M. Wingen, B. J. Finlayson-Pitts, Integrating phase and composition of secondary organic aerosol from the ozonolysis of α-pinene. *Proc. Natl. Acad. Sci. U.S.A.* **111**, 7552–7557 (2014).
9. P. Liu *et al.*, Lability of secondary organic particulate matter. *Proc. Natl. Acad. Sci. U.S.A.* **113**, 12643–12648 (2016).
10. A. C. Vander Wall, V. Perraud, L. M. Wingen, B. J. Finlayson-Pitts, Evidence for a kinetically controlled burying mechanism for growth of high viscosity secondary organic aerosol. *Environ. Sci. Process. Impacts* **22**, 66–83 (2020).
11. L. Renbaum-Wolff *et al.*, Viscosity of α-pinene secondary organic material and implications for particle growth and reactivity. *Proc. Natl. Acad. Sci. U.S.A.* **110**, 8014–8019 (2013).
12. M. Shiraiwa *et al.*, Global distribution of particle phase state in atmospheric secondary organic aerosols. *Nat. Commun.* **8**, 15002 (2017).
13. A. M. Maclean *et al.*, Humidity-dependent viscosity of secondary organic aerosol from ozonolysis of β-caryophyllene: Measurements, predictions, and implications. *ACS Earth Space Chem.* **5**, 305–318 (2021).
14. T. Koop, J. Bookhold, M. Shiraiwa, U. Pöschl, Glass transition and phase state of organic compounds: Dependency on molecular properties and implications for secondary organic aerosols in the atmosphere. *Phys. Chem. Chem. Phys.* **13**, 19238–19255 (2011).
15. Y. Qin *et al.*, Humidity dependence of the condensational growth of α-pinene secondary organic aerosol particles. *Environ. Sci. Technol.* **55**, 14360–14369 (2021).
16. R. A. Zaveri *et al.*, Growth kinetics and size distribution dynamics of viscous secondary organic aerosol. *Environ. Sci. Technol.* **52**, 1191–1199 (2018).
17. Y. Han *et al.*, Quantifying the role of the relative humidity-dependent physical state of organic particulate matter in the uptake of semivolatile organic molecules. *Environ. Sci. Technol.* **53**, 13209–13218 (2019).
18. C. Denjean *et al.*, Relating hygroscopicity and optical properties to chemical composition and structure of secondary organic aerosol particles generated from the ozonolysis of α-pinene. *Atmos. Chem. Phys.* **15**, 3339–3358 (2015).
19. P. E. Ohno *et al.*, Fluorescence aerosol flow tube spectroscopy to detect liquid-liquid phase separation. *ACS Earth Space Chem.* **5**, 1223–1232 (2021).
20. F. Mahrt *et al.*, Phase behavior of internal mixtures of hydrocarbon-like primary organic aerosol and secondary aerosol based on their differences in oxygen-to-carbon ratios. *Environ. Sci. Technol.* **56**, 3960–3973 (2022).
21. M. A. Freedman, Liquid-liquid phase separation in supermicrometer and submicrometer aerosol particles. *Acc. Chem. Res.* **53**, 1102–1110 (2020).
22. K. Kristensen *et al.*, High-molecular weight dimer esters are major products in aerosols from α-pinene ozonolysis and the boreal forest. *Environ. Sci. Technol. Lett.* **3**, 280–285 (2016).
23. X. Zhang *et al.*, Formation and evolution of molecular products in α-pinene secondary organic aerosol. *Proc. Natl. Acad. Sci. U.S.A.* **112**, 14168–14173 (2015).
24. S. A. Nizkorodov, J. Laskin, A. Laskin, Molecular chemistry of organic aerosols through the application of high resolution mass spectrometry. *Phys. Chem. Chem. Phys.* **13**, 3612–3629 (2011).
25. P. F. DeCarlo *et al.*, Field-deployable, high-resolution, time-of-flight aerosol mass spectrometer. *Anal. Chem.* **78**, 8281–8289 (2006).
26. A. Zelenyuk, D. Imre, Single particle laser ablation time-of-flight mass spectrometer: An introduction to SPLAT. *Aerosol Sci. Technol.* **39**, 554–568 (2005).
27. K. A. Pratt, K. A. Prather, Mass spectrometry of atmospheric aerosols–recent developments and applications. Part II: On-line mass spectrometry techniques. *Mass Spectrom. Rev.* **31**, 17–48 (2012).
28. M. V. Johnston, S. Wang, M. S. Reinard, Nanoparticle mass spectrometry: Pushing the limit of single particle analysis. *Appl. Spectrosc.* **60**, 264–272 (2006).
29. J. N. Smith, K. F. Moore, P. H. McMurry, F. L. Eisele, Atmospheric measurements of sub-20 nm diameter particle chemical composition by thermal desorption chemical ionization mass spectrometry. *Aerosol Sci. Technol.* **38**, 100–110 (2004).
30. P. J. Gallimore, M. Kalberer, Characterizing an extractive electrospray ionization (EESI) source for the online mass spectrometry analysis of organic aerosols. *Environ. Sci. Technol.* **47**, 7324–7331 (2013).
31. H. Chen, A. Venter, R. G. Cooks, Extractive electrospray ionization for direct analysis of undiluted urine, milk and other complex mixtures without sample preparation. *Chem. Commun. (Camb.)* **19**, 2042–2044 (2006).
32. A. J. Horan, Y. Gao, W. A. Hall IV, M. V. Johnston, Online characterization of particles and gases with an ambient electrospray ionization source. *Anal. Chem.* **84**, 9253–9258 (2012).
33. J. T. Jayne *et al.*, Aerosol mass spectrometer for size and composition analysis of submicron particles. *J. Aerosol Sci.* **29**, 49–70 (1998).
34. D. M. Murphy, D. S. Thomson, Laser ionization mass spectroscopy of single aerosol particles. *Aerosol Sci. Technol.* **22**, 237–249 (1995).
35. M. N. Chan, T. Nah, K. R. Wilson, Real time in situ chemical characterization of sub-micron organic aerosols using Direct Analysis in Real Time mass spectrometry (DART-MS): The effect of aerosol size and volatility. *Analyst (Lond.)* **138**, 3749–3757 (2013).
36. S. Kumbhani *et al.*, New mechanism of extractive electrospray ionization mass spectrometry for heterogeneous solid particles. *Anal. Chem.* **90**, 2055–2062 (2018).
37. T. Nah, M. Chan, S. R. Leone, K. R. Wilson, Real time in situ chemical characterization of submicrometer organic particles using direct analysis in real time-mass spectrometry. *Anal. Chem.* **85**, 2087–2095 (2013).
38. L. M. Wingen, B. J. Finlayson-Pitts, Probing surfaces of atmospherically relevant organic particles by easy ambient sonic-spray ionization mass spectrometry (EASI-MS). *Chem. Sci. (Camb.)* **10**, 884–897 (2018).
39. S. Trimpin, "Magic" ionization mass spectrometry. *J. Am. Soc. Mass Spectrom.* **27**, 4–21 (2016).
40. S. Trimpin, E. D. Inutan, Matrix assisted ionization in vacuum, a sensitive and widely applicable ionization method for mass spectrometry. *J. Am. Soc. Mass Spectrom.* **24**, 722–732 (2013).

41. S. Trimpin et al., New ionization processes and applications for use in mass spectrometry. *Crit. Rev. Biochem. Mol. Biol.* **48**, 409–429 (2013).
42. S. Trimpin et al., Spontaneous charge separation and sublimation processes are ubiquitous in nature and in ionization processes in mass spectrometry. *J. Am. Soc. Mass Spectrom.* **29**, 304–315 (2018).
43. S. Trimpin, M. Pophristic, A. Adeniji-Adele, J. W. Tomsho, C. N. McEwen, Vacuum matrix-assisted ionization source offering simplicity, sensitivity, and exceptional robustness in mass spectrometry. *Anal. Chem.* **90**, 11188–11192 (2018).
44. M. J. Apsokardu, J. M. Krasnomowitz, S. Jiang, M. V. Johnston, Ion formation from rapidly heated aqueous droplets by droplet-assisted ionization. *J. Phys. Chem. A* **124**, 7313–7321 (2020).
45. D. E. Kerecman et al., Online characterization of organic aerosol by condensational growth into aqueous droplets coupled with droplet-assisted ionization. *Anal. Chem.* **93**, 2793–2801 (2021).
46. M. J. Apsokardu, D. E. Kerecman, M. V. Johnston, Ion formation in droplet-assisted ionization. *Rapid Commun. Mass Spectrom.* **35** (suppl. 1), e8227 (2021).
47. S. Trimpin et al., A mechanism for ionization of nonvolatile compounds in mass spectrometry: Considerations from MALDI and inlet ionization. *J. Am. Soc. Mass Spectrom.* **23**, 1644–1660 (2012).
48. V. S. Pagnotti, N. D. Chubatyi, C. N. McEwen, Solvent assisted inlet ionization: An ultrasensitive new liquid introduction ionization method for mass spectrometry. *Anal. Chem.* **83**, 3981–3985 (2011).
49. M. A. Fenner, C. N. McEwen, Survival yield comparison between ESI and SAII: Mechanistic implications. *Int. J. Mass Spectrom.* **378**, 107–112 (2015).
50. V. V. Pervukhin, D. G. Sheven, Aerodynamic thermal breakup droplet ionization in mass spectrometric drug analysis. *J. Am. Soc. Mass Spectrom.* **31**, 1074–1082 (2020).
51. V. V. Pervukhin, D. G. Sheven, Using of aerodynamic droplet breakup for mass-spectrometric analysis. *Talanta* **185**, 7–15 (2018).
52. L. W. Zilch, J. T. Maze, J. W. Smith, G. E. Ewing, M. F. Jarrold, Charge separation in the aerodynamic breakup of micrometer-sized water droplets. *J. Phys. Chem. A* **112**, 13352–13363 (2008).
53. M. Domin, R. Cody, Eds., *Ambient Ionization Mass Spectrometry* (The Royal Society of Chemistry, 2015).
54. J. Greaves, J. Roboz, *Mass Spectrometry for the Novice* (CRC Press, 2008).
55. J. Li et al., Matrix assisted ionization: New aromatic and nonaromatic matrix compounds producing multiply charged lipid, peptide, and protein ions in the positive and negative mode observed directly from surfaces. *J. Am. Soc. Mass Spectrom.* **23**, 1625–1643 (2012).
56. G. A. Somorjai, Mechanism of sublimation. *Science* **162**, 755–760 (1968).
57. S. M. A. Malek, V. Kwan, I. Saika-Voivod, S. Consta, Low density interior in supercooled aqueous nanodroplets expels ions to the subsurface. *J. Am. Chem. Soc.* **143**, 13113–13123 (2021).
58. U. Molteni et al., Formation of highly oxygenated organic molecules from α-pinene ozonolysis: Chemical characteristics, mechanism, and kinetic model development. *ACS Earth Space Chem.* **3**, 873–883 (2019).
59. W. A. Hall, M. V. Johnston, Oligomer formation pathways in secondary organic aerosol from MS and MS/MS measurements with high mass accuracy and resolving power. *J. Am. Soc. Mass Spectrom.* **23**, 1097–1108 (2012).
60. B. Forsyth, B. Y. H. Liu, F. J. Romay, Particle charge distribution measurement for commonly generated laboratory aerosols. *Aerosol Sci. Technol.* **28**, 489–501 (1998).
61. C. J. Tsai, J. S. Lin, C. G. Deshpande, L. C. Liu, Electrostatic charge measurement and charge neutralization of fine aerosol particles during the generation process. *Part. Part. Syst. Charact.* **22**, 293–298 (2006).
62. V. V. Pervukhin, D. G. Sheven', Y. N. Kolomiets, Collison nebulizer as a new soft ionization source for mass spectrometry. *Tech. Phys.* **61**, 1262–1268 (2016).
63. L. B. Loeb, *Static Electrification* (Springer, 1958).
64. W. C. Hinds, *Aerosol Technology: Properties, Behavior, and Measurement of Airborne Particles* (Wiley, New York, NY, ed. 2, 1999).
65. M. Bilde et al., Saturation vapor pressures and transition enthalpies of low-volatility organic molecules of atmospheric relevance: From dicarboxylic acids to complex mixtures. *Chem. Rev.* **115**, 4115–4156 (2015).
66. J. V. Iribarne, B. A. Thomson, On the evaporation of small ions from charged droplets. *J. Chem. Phys.* **64**, 2287–2294 (1976).
67. M. Dole et al., Molecular beams of macroions. *J. Chem. Phys.* **49**, 2240–2249 (1968).
68. I. G. Loscertales, J. Fernández De La Mora, Experiments on the kinetics of field evaporation of small ions from droplets. *J. Chem. Phys.* **103**, 5041–5060 (1995).
69. C. J. Hogan Jr., J. Fernandez de la Mora, Ion-pair evaporation from ionic liquid clusters. *J. Am. Soc. Mass Spectrom.* **21**, 1382–1386 (2010).
70. P. Kebarle, M. Peschke, On the mechanisms by which the charged droplets produced by electrospray lead to gas phase ions. *Anal. Chim. Acta* **406**, 11–35 (2000).
71. S. Consta, Direct evidence of jets emanating from droplets at the Rayleigh charge-induced instability point. arXiv [Preprint] (2021). https://doi.org/10.48550/arXiv.2106.03756.
72. V. Kwan, A. Malevanets, S. Consta, Where do the ions reside in a highly charged droplet? *J. Phys. Chem. A* **123**, 9298–9310 (2019).
73. S. Consta, A. Malevanets, Manifestations of charge induced instability in droplets effected by charged macromolecules. *Phys. Rev. Lett.* **109**, 148301 (2012).
74. P. Kebarle, U. H. Verkerk, Electrospray: From ions in solution to ions in the gas phase, what we know now. *Mass Spectrom. Rev.* **28**, 898–917 (2009).
75. V. Kwan, S. Consta, Bridging electrostatic properties between nanoscopic and microscopic highly charged droplets. *Chem. Phys. Lett.* **746**, 137238 (2020).
76. A. Roose, C. Toubin, S. Dusanter, V. Riffault, D. Duflot, Classical molecular dynamics study of small-chain carboxylic acid aerosol particles. *ACS Earth Space Chem.* **3**, 380–389 (2019).
77. J. Latham, B. J. Mason, Electric charge transfer associated with temperature gradients in ice. *Proc. R. Soc. Lond. A Math. Phys. Sci.* **260**, 523–536 (1961).
78. J. Latham, C. D. Stow, Electrification associated with the evaporation of ice. *J. Atmos. Sci.* **22**, 320–324 (1965).
79. N. Agmon, The Grotthuss mechanism. *Chem. Phys. Lett.* **244**, 456–462 (1995).
80. S. Cukierman, Et tu, Grotthuss! and other unfinished stories. *Biochim. Biophys. Acta* **1757**, 876–885 (2006).
81. M. Petters, S. Kasparoglu, Predicting the influence of particle size on the glass transition temperature and viscosity of secondary organic material. *Sci. Rep.* **10**, 15170 (2020).
82. P. Pradeep Kumar, K. Broekhuizen, J. P. D. Abbatt, Organic acids as cloud condensation nuclei: Laboratory studies of highly soluble and insoluble species. *Atmos. Chem. Phys.* **3**, 509–520 (2003).
83. C. N. Cruz, S. N. Pandis, Deliquescence and hygroscopic growth of mixed inorganic–Organic atmospheric aerosol. *Environ. Sci. Technol.* **34**, 4313–4319 (2000).
84. Y. Qin, L. Wingen, B. Finlayson-Pitts, Toward a molecular understanding of the surface composition of atmospherically relevant organic particles. DRYAD. https://datadryad.org/stash/dataset/doi:10.7280/D1Z41R. Accessed 12 August 2022.